



CHORUS

This is the accepted manuscript made available via CHORUS. The article has been published as:

Oxygen Quadclusters in SiO₂ Glass above Megabar Pressures up to 160 GPa Revealed by X-Ray Raman Scattering

Sung Keun Lee, Yong-Hyun Kim, Yoo Soo Yi, Paul Chow, Yuming Xiao, Cheng Ji, and Guoyin Shen

Phys. Rev. Lett. **123**, 235701 — Published 5 December 2019

DOI: [10.1103/PhysRevLett.123.235701](https://doi.org/10.1103/PhysRevLett.123.235701)

Oxygen Quadclusters in SiO₂ Glass above Megabar Pressures up to 160 GPa revealed by X-ray Raman Scattering

Sung Keun Lee^{1,2*}, Yong-Hyun Kim¹, Yoo Soo Yi¹, Paul Chow³, Yuming Xiao³, Cheng Ji⁴, Guoyin Shen^{3*}

¹*School of Earth and Environmental Sciences, Seoul National University, Seoul, 08826 Korea*

²*Institute of Applied Physics, Seoul National University, Seoul, 08826 Korea*

³*HPCAT, X-ray Science Division, Argonne National Laboratory, Argonne, IL 60439, USA*

⁴*Geophysical Laboratory, Carnegie Institution for Science, Argonne, IL 60439, USA*

*Corresponding author. Email: sungklee@snu.ac.kr gyshen@anl.gov

ABSTRACT

As oxygen may occupy a major volume of oxides, a densification of amorphous oxides under extreme compression is dominated by reorganization of oxygen during compression. Here, X-ray Raman scattering spectra (XRS) for SiO₂ glass up to 1.6 megabar reveal the evolution of heavily contracted oxygen environments characterized by a decrease in average O-O distance and the emergence of quadruply coordinated oxygen (oxygen quadcluster). Our results also reveal that the edge energies at the centers of gravity of the XRS features increase *linearly* with bulk density, yielding the first predictive relationship between the density and partial density of state of oxides above megabar pressures. The extreme densification paths with densified oxygen in amorphous oxides shed light upon possible existence of stable melts in the planetary interiors.

Compressed glasses that undergo densification *far above* megabar pressures (i.e., pressures above 100 GPa) may consist of heavily entangled amorphous structures that are different from those at lower pressures, as well as from those observed in crystalline analogues. While the structures of major crystals in Earth's mantle at pressures greater than 100 GPa are well understood, the atomic configurations of non-crystalline silicates at the bottom of the mantle at pressures of ~130 GPa remain unclear due to experimental difficulties[1,2]. Furthermore, considering much larger radii of the super-Earths, the silicate parts in those planetary bodies are extended into much higher pressure conditions. The detailed structures of silicate melts at the pressure conditions much higher than that of Earth's lower mantle remains elusive.

Known as the prototypical amorphous oxide, SiO₂ glass (*a*-SiO₂) may give rise to a diverse roster of bonding configurations when compressed beyond megabar pressures. *a*-SiO₂ is also a major component of technologically important oxide glasses and yields atomistic insights into the differentiation of the primitive mantle from the magma ocean and the evolution of super-Earths[3]. The structural changes in *a*-SiO₂ at high pressure provide simplified yet essential densification paths for complex silicates, including SiO₂-rich melts at the bottom of Earth's mantle and that of other Super-Earth bodies[2-6] and are responsible for the anomalous pressure dependence of the elastic properties of *a*-SiO₂ under compression[7].

The densification in silicates has traditionally been described in terms of how cations are rearranged under compression (e.g., the Si coordination number)[8-10]. However, in a simplified model of ionic oxide, considering its much larger ionic radius, oxygen (with an ionic radius of ~1.4 Å, compared with that of 0.28 Å for Si) – the most abundant element in bulk silicate Earth – occupies a major volume of oxides. The degree of oxide densification at high pressure is likely to be dominated by the reorganization of oxygen during compression (Supplemental Material, S1). While the nature of oxygen in *a*-SiO₂ undergoing densification is enigmatic, the average Si coordination number of *a*-SiO₂ increases with increasing pressure, forming highly coordinated Si (^{5,6}Si) [3,7,10-13](S2). The formation of ^{5,6}Si in *a*-SiO₂ is accompanied by the formation of *triply* coordinated oxygen (³O, oxygen triclusters)[14] from *doubly* coordinated bridging oxygen (⁴Si-²O-⁴Si)(S1). Elastic X-ray scattering measurements of *a*-SiO₂ have indicated that the average coordination number of Si may be larger than 6 near 100 GPa, reaching up to ~6.9 at 170 GPa [12] (Figure S1). This implies that in addition to ³O, other highly coordinated oxygen may form above 1.2 megabar pressures. The potential presence and the electronic structures of oxygen beyond ³O in amorphous oxides need to be confirmed. Information regarding oxygen-specific changes occurring under compression will resolve the puzzle of the glass structure under well beyond-megabar pressures, constraining the densification mechanisms of amorphous oxides.

Despite the importance, previous efforts to identify the direct *oxygen-specific* configurations of *a*-SiO₂ and silicate glasses well above megabar pressures have remained challenging (S2). X-ray Raman scattering (XRS) reveals local electronic bonding environments around oxygen in diverse oxides through the partial electronic density of states (PDOS) [14-20]. Key to the successful application of XRS studies under megabar pressure conditions is the efficient capture of inelastically scattered photons from compressed samples while minimizing the background signals from the gaskets used to sustain the high-pressure conditions [21,22]. However, the XRS process is inefficient, as it yields signal intensity that is 3-6 orders of magnitude smaller than that of elastic X-rays

(S3). Recent advances in the post-collimation of inelastically scattered X-rays shed light on an opportunity to collect high-resolution XRS signals under extreme compression[17], while the inherent inefficiency limits the maximum pressure conditions for the collection of inelastic scattering x-rays of any condensed matter to ~ 120 GPa. In the current study, the experimental breakthrough allows us to collect the XRS signal of contracted oxygens in *a*-SiO₂ well above megabar pressures up to 160 GPa. We provide spectroscopic proxies based on O *K*-edge XRS from which to infer the densification of silicate melts far beyond megabar pressures.

The *a*-SiO₂ (Corning, FS7980) was loaded into a panoramic diamond anvil cell using a beryllium gasket (S4 for detailed experimental conditions[17]). The diamond culet for the experiment up to 124 GPa is 150 μm and that at higher pressure up to 160 GPa is 110 μm . The Be gasket was pre-indented with a hole diameter of ~ 40 -60 μm . Oxygen *K*-edge XRS spectra for the *a*-SiO₂ were collected at the HPCAT beamline 16-ID-D at the Advanced Photon Source. The XRS spectra were collected by scanning the incident photon energy relative to the analyzer energy of 9.908 keV. The incident X-rays were produced by a double-crystal Si(111) monochromator. KB mirrors and a pin-hole upstream of the sample focus a beam with a FWHM of 8(horizontal) \times 5(vertical) μm^2 . A poly-capillary (PC) post-collimation optics was combined with a single spherical Si(555) analyzer, with an Amptek silicon detector. A PC with a 7 mm working distance and collection cone angle of 12° was employed [17,21], making the scattering angle vary from 19° to 31°. The Raman signal from the diamond culet was used to estimate the pressure [23]. The pressure variation within the sample chamber at high pressure conditions is up to ~ 10 GPa (S4). The spectra were collected from 1 atm to 160 GPa with varying energy loss (incident energy–elastic energy) from 530 to 565 eV.

The oxygen *K*-edge XRS spectra for *a*-SiO₂ at high pressures up to 160 GPa exhibit a series of pressure-induced changes in edge features centered at ~ 538 , ~ 544 , and ~ 548 eV (Figure 1;S5), revealing dramatic changes in the oxygen environments under compression. The spectrum at 1 atm shows a broad peak at 538 eV that represents the transition of a core electron to a σ^* antibonding $2p$ state in ¹⁶O coordinated with two ²⁸Si frameworks (S6). The spectrum also shows a minor shoulder at ~ 545 eV, consistent with an earlier O *K*-edge XRS spectrum[14,19]. The main σ^* peak shifts to high energy with increasing pressure. At pressures of ~ 24 GPa, a major spectral feature at ~ 544 -545 eV appears, with its intensity increasing as pressure increases up to ~ 80 GPa. The systematic increase in the absorption threshold (dotted line) corresponds to a decrease in the average O-O distance ($d_{\text{O-O}}$)

[24,25](S6). Furthermore, the fraction of $^{[3]}\text{O}$ gradually increases as pressure increases, similar to the results from *ab initio* molecular dynamics (MD) simulations of *a*- SiO_2 [26] (S2). Thus, the formation of $^{[3]}\text{O}$ and the variations in the short-to-medium-range structures accompanying the growth of $^{[3]}\text{O}$ contribute to the feature at ~ 544 eV [15].

The XRS spectrum at 100 GPa reveals the emergence of an additional feature at ~ 548 eV. Its intensity is more prominent in the spectrum at 124 GPa. With a further increase in pressure, the spectra collected at 140 GPa and 160 GPa revealed an increase in the high energy features. This feature indicates that an additional densification of the amorphous networks other than the formation of $^{[3]}\text{O}$ may prevail above megabar pressures. The O *K*-edge XRS features could be due to diverse structural changes associated with the densification (S5): as the average coordination number of Si in this pressure range is larger than 6 (S2), this feature indicates the evolution of oxygen configurations involving quadruply coordinated oxygen ($^{[4]}\text{O}$, oxygen quadclusters) and a significant reduction in oxygen proximity. Multiple structural arrangements around $^{[4]}\text{O}$ resulting from the distribution of $^{[5,6,7]}\text{Si}$ around the highly coordinated oxygens explain the features observed at 548 eV. The *K*-edge features at higher pressures are also broader than those at 1 atm, indicating an increase in dispersion in the O-*2p* and O-*d* PDOS of the compressed oxygen [24,25]. This dispersion results from more complex atomic configurations [e.g., $^{[3,4]}\text{O}$ with varying Si coordination states ($^{[5,6,7]}\text{Si}$)] around the oxygen and wider O-O distribution at high pressure. The distortion of Si polyhedra involving $^{[4]}\text{O}$ and, thus, the Si-O bond-length distribution is likely to be more prominent well above megabar pressures[27]. This indicates that the extent of structural disorder in *a*- SiO_2 increases above megabar pressures. Because melt viscosity at high pressure decreases with increasing configurational entropy of melts[28], the pressure-induced changes in structural disorder associated with emergence of $^{[4]}\text{O}$ suggest a decrease in melt viscosity in the bottom of the mantle.

To elaborate the oxygen environments in *a*- SiO_2 under extreme compression, the O *K*-edge XRS spectra for *a*- SiO_2 are compared with those calculated for crystalline phases (Figures 2 and S3; the simulation methods are presented in S7). With increasing pressure, crystalline SiO_2 undergoes phase transitions from quartz (1 atm) and stishovite (~ 9.3 GPa) to higher-pressure phases, including α - PbO_2 -type at ~ 120 GPa [29-32]. The edge features and the absorption threshold for these crystalline phases both shift to higher energy (~ 4 - 5 eV) as the pressure increases up to 120 GPa, consistent with the trend observed for MgSiO_3 phases [24,25]. The main peak at 538 eV for quartz is similar to that for the *a*- SiO_2 at 1 atm. The doublet-like feature at ~ 536 and 543 eV in stishovite at 29 GPa is characteristic of $^{[3]}\text{O}$ linking three $^{[6]}\text{Si}$ atoms in an edge-sharing topology [24,25], similar to the feature for the *a*-

SiO₂ at 24 GPa (Figure 1). The calculated spectrum for the α -PbO₂ phase at 120 GPa reveals a feature at 546-548 eV, indicating a further reduction in average d_{O-O} (S8).

The observed changes in the O *K*-edge features for the crystalline phases and *a*-SiO₂ reveal the structural adaptation of the oxides upon densification. In particular, the edge energies at the centers of gravity (E_c) of the main σ^* features of the diverse crystalline phases and the *a*-SiO₂ increase upon compression (Figures 3A; Figures S4-S5, see S9 for the calculation of E_c). Because the average d_{O-O} values in crystalline silica systematically decrease with pressure (Tables S1 and S2), the E_c increases with a decreasing average d_{O-O} [i.e., $E_c(\text{eV}) \approx -14.4 \times d_{\text{O-O}}(\text{\AA}) + 577.4$] (Figure 3B). Therefore, E_c can be regarded as a measure of oxygen proximity for oxide densification under extreme compression at *beyond*-megabar pressures. Based on the trend, an observed shift in the σ^* peak in *a*-SiO₂ corresponds to a decrease in d_{O-O} of ~ 0.35 \AA at pressures up to ~ 124 GPa, which is comparable to the estimated decrease due to densification (and an increase in the oxygen packing density) in the crystalline phases (~ 0.3 \AA) [the difference between the d_{O-O} of quartz (2.6261 \AA) and that of α -PbO₂ (2.3273 \AA)] [9] (S5; Table S2). We also found that the increase in E_c is well correlated with the increase in the bulk density (ρ) of *a*-SiO₂ (Figure 3C). Here, we used the density of *a*-SiO₂ as obtained from a pioneering X-ray absorption study [33]. As the E_c values depend on the way in which the peak positions were determined (S9), the results provide a semi-quantitative trend. Nevertheless, the relationship can be described by the following linear equation: $E_c(\text{eV}) \approx 1.6 \times \rho + 536.6$, revealing the predictive relationship between the glass density and partial density of state of oxides above megabar pressures. The current results establish the first simple relationship between the density, the oxygen proximity [i.e., d_{O-O}], and a shift in the O *K*-edge energy (parameterized by E_c). Both the oxygen proximity and E_c (experimentally measurable quantity) can be used as novel proxies for the densification of oxides at high pressures up to 160 GPa.

The average Si coordination number (C_{Si}) in *a*-SiO₂ increases from 4 to 6 with increasing pressure up to ~ 100 GPa [10,11,13]. C_{Si} is greater than 6 at high pressures above ~ 100 GPa, forming ⁷Si (S2) [12]. Considering the relationship between cation coordination number and the average oxygen coordination number (C_{O}) in *a*-SiO₂, i.e., $C_{\text{Si}} = 2 \times C_{\text{O}}$ [34-36], the C_{O} in *a*-SiO₂ above megabar pressures is larger than 3. Figure 4 shows the average oxygen coordination number values calculated from the average Si coordination number from experimental studies [11-13,37] (S2). Formation of oxygen triclusters (³[^{5,6}Si-³O]) in *a*-SiO₂ below 100 GPa results from a pressure-induced chemical bonding between ²O and ^{4,5}Si. Above megabar pressures, oxygen quadclusters (e.g., ⁴[^{6,7}Si-⁴O]) form through the annihilation of ³O and ⁶Si (e.g., $3[\sup{6}\text{Si}-\sup{3}\text{O}] + \sup{6}\text{Si} \rightarrow 4[\sup{6,7}\text{Si}-\sup{4}\text{O}]$), and the fraction of ⁴O is expected to gradually increase as pressure increases. At ~ 120 GPa, considering the estimated C_{O} value of 3.25 [12] (assuming the presence only of ^{3,4}O above megabar

pressures, and thus the absence of $^{[2]}\text{O}$), $\sim 75\%$ of the oxygen exists in the form of $^{[3]}\text{O}$, while $\sim 25\%$ of the oxygen is present as $^{[4]}\text{O}$ (i.e., $0.25 \times 4 + 0.75 \times 3 = 3.25$). Furthermore, at ~ 160 GPa, the C_{O} value can be ~ 3.4 [12]. Then, $\sim 60\%$ of the oxygen exists in the form of $^{[3]}\text{O}$, while $\sim 40\%$ of the oxygen is present as $^{[4]}\text{O}$ (i.e., $0.4 \times 4 + 0.6 \times 3 = 3.4$). The changes in the O K -edge XRS features in $a\text{-SiO}_2$ and the E_c are well-correlated with C_{O} and the spectral evolutions up to 1.6 megabar pressures may indicate the formation of $^{[4]}\text{O}$ [27]. As the C_{Si} from the theoretical calculations is somewhat lower[7,27], a quantitative fraction of $^{[4]}\text{O}$ remains to be confirmed(S2). A complementary view of the oxygen coordination transformation in oxides was provided in an earlier model from O'Keefe[38-40] where the changes in electronic structures around oxygen upon compression are determined by varying numbers of the nearest neighbor Si. The hindrance to form highly coordinated oxygen stems from the repulsive Si...Si interactions. The degree of densification can be described with distance between Si's, while $d_{\text{O-O}}$ was used to describe the densification in amorphous oxides in the current study. The linear relationship between oxygen PDOS and the bulk density indicates a collective nature of oxygen PDOS that reflects short-to-intermediate range configurations around oxygen[24,25]. A low-energy vibrational density of states also correlates well with the density of $a\text{-SiO}_2$ because of its collective nature[41].

The current experimental breakthroughs with oxygen-specific XRS spectra for $a\text{-SiO}_2$ up to 1.6 megabars allow us to draw conclusions regarding the oxygen bonding nature in amorphous oxides under compression that differ from those of crystals. Densification in crystalline silica under compression is achieved through changes in long-range topological rearrangements upon phase transition without coordination transformation up to 160 GPa. For example, the $\alpha\text{-PbO}_2$ phase has coordination environments similar to those of lower-pressure phases (the CaCl_2 -type phase and stishovite): all these phases consist of $^{[6]}\text{Si}$ and $^{[3]}\text{O}$. In contrast, densification in $a\text{-SiO}_2$ results in gradual changes in short-range configurations and the formation of more highly coordinated configurations, including $^{[7]}\text{Si}$ and $^{[4]}\text{O}$, above megabar pressures up to 160 GPa. The oxygen-specific densification path is characterized by the formation of oxygen quadclusters, making the $^{[4]}\text{O}$ fraction a new indicator of melt densification.

The behaviour of $a\text{-SiO}_2$ under compression gives clues about how densification occurs for non-crystalline silicates in Earth and planetary interiors. Note that the dense partial melts have additional components, such as MgO, FeO and/or H_2O [42-44]. In such melts, the formation of highly coordinated oxygen becomes more complex, as average Si and oxygen coordination numbers of the Mg-rich melts are smaller than those of SiO_2 liquids [45,46](S1). Further experimental efforts for complex silicate melts at an elevated temperature conditions are required. Nevertheless, along with the silica-rich nature of the proposed partial melts in ULVZ[4], the current densification model for $a\text{-SiO}_2$ can be

applied to account for the unusual stability and structural transformation in complex melts at the CMB[47], as SiO₂ is a major endmember of any magma composition. Densified deep mantle melts consisting primarily of ^{3,4}O configurations result in enhanced topological contraction, providing a potential path for extreme melt densification at the CMB and the negative buoyancy of such melts in deep magma ocean and that in the Super-Earths.

Finally, while O *K*-edge XRS is a unique probe of the electronic density of states of crystalline and amorphous materials at high pressures, the pressure-induced changes in the spectra up to ~50 GPa are subtle, so the full utility of the XRS technique has not often been demonstrated in previous applications. The current study of silica at pressures up to 160 GPa shows that the XRS spectrum changes drastically with extreme compression, so this technique is suitable for use in studying the detailed bonding under compression at beyond-megabar pressures. The conceptual advances (i.e., oxygen-specific densification mechanism, electronic density of state *vs.* bulk density above megabar pressure conditions) and experimental breakthroughs allow us to account for the densification in an enormous number of glass-forming oxides. Despite the unsurmountable challenges that lie ahead for XRS techniques, the current results offer inspiration for the application of XRS studies of complex glasses, as well as crystals under multi-megabar pressure conditions.

ACKNOWLEDGMENTS We thank three anonymous reviewers for constructive suggestions which improved the manuscript's quality. This work was supported by National Research Foundation, Korea (2017R1A2A1A17069511) and the Samsung Science and Technology Foundation (SSTF) (BA1401-07) to S.K.L. G. Shen acknowledges the support by DOE-BES, Division of Materials Sciences and Engineering under Award DE-FG02-99ER45775. HPCAT operations are supported by DOE-NNSA's Office of Experimental Sciences. The Advanced Photon Source is a User Facility operated for the DOE Office of Science by Argonne National Laboratory under Contract No. DE-AC02-06CH11357.

REFERENCES

- [1] R. J. Hemley, V. V. Struzhkin, R. E. Cohen, and G. Shen, in *Treatise on Geophysics (Second Edition)*, edited by G. Schubert (Elsevier, Oxford, 2015), pp. 313.
- [2] T. Lay, in *Treatise on Geophysics (Second Edition)*, edited by G. Schubert (Elsevier, Oxford, 2015), pp. 683.
- [3] B. B. Karki, D. Bhattarai, and L. Stixrude, *Phys. Rev. B* **76**, 104205 (2007).
- [4] D. Andrault, G. Pesce, M. A. Bouhifd, B. N. Casanova, J. M. Hénot, and M. Mezouar, *Science* **344**, 892 (2014).
- [5] M. Murakami and J. D. Bass, *Phys. Rev. Lett.* **104**, 025504 (2010).
- [6] R. Scipioni, L. Stixrude, and M. P. Desjarlais, *Proc. Natl. Acad. Sci. USA* **114**, 9009 (2017).
- [7] M. Wu, Y. Liang, J.-Z. Jiang, and J. S. Tse, *Sci. Rep.* **2**, 398 (2012).
- [8] Y. Wang *et al.*, *Nat. Commun.* **5**, 3241 (2014).
- [9] A. Zeidler, P. S. Salmon, and L. B. Skinner, *Proc. Natl. Acad. Sci. USA* **111**, 10045 (2014).
- [10] A. Zeidler *et al.*, *Phys. Rev. Lett.* **113**, 135501 (2014).
- [11] C. J. Benmore, E. Soignard, S. A. Amin, M. Guthrie, S. D. Shastri, P. L. Lee, and J. L. Yarger, *Phys. Rev. B* **81**, 054105 (2010).
- [12] C. Prescher, V. B. Prakapenka, J. Stefanski, S. Jahn, L. B. Skinner, and Y. Wang, *Proc. Natl. Acad. Sci. USA* **114**, 10041 (2017).
- [13] T. Sato and N. Funamori, *Phys. Rev. B* **82**, 184102 (2010).
- [14] S. K. Lee *et al.*, *Proc. Natl. Acad. Sci. USA* **105**, 7925 (2008).
- [15] S. K. Lee, P. J. Eng, and H. K. Mao, in *Spectroscopic Methods in Mineralogy and Materials Sciences*, edited by G. S. Henderson, D. R. Neuville, and R. T. Downs (Mineralogical Society of America, Washington, D.C., 2014), pp. 139.
- [16] S. K. Lee, P. J. Eng, H. K. Mao, Y. Meng, M. Newville, M. Y. Hu, and J. F. Shu, *Nat. Mater.* **4**, 851 (2005).
- [17] S. K. Lee, Y.-H. Kim, P. Chow, Y. Xiao, C. Ji, and G. Shen, *Proc. Natl. Acad. Sci. USA* **115**, 5855 (2018).
- [18] G. Lelong, L. Cormier, G. Ferlat, V. Giordano, G. S. Henderson, A. Shukla, and G. Calas, *Phys. Rev. B* **85**, 134202 (2012).
- [19] J. F. Lin *et al.*, *Phys. Rev. B* **75**, 012201 (2007).
- [20] C. Sternemann and M. Wilke, *High Press. Res.* **36**, 275 (2016).
- [21] P. Chow, Y. M. Xiao, E. Rod, L. G. Bai, G. Y. Shen, S. Sinogeikin, N. Gao, Y. Ding, and H.-K. Mao, *Rev. Sci. Instrum.* **86**, 072203 (2015).
- [22] S. Petitgirard *et al.*, *Geochem. Persp. Lett.* **9**, 32 (2019).
- [23] Y. Akahama and H. Kawamura, *High Press. Res.* **27**, 473 (2007).
- [24] Y. S. Yi and S. K. Lee, *Am. Mineral.* **97**, 897 (2012).
- [25] Y. S. Yi and S. K. Lee, *Phys. Rev. B* **94**, 094110 (2016).
- [26] A. Trave, P. Tangney, S. Scandolo, A. Pasquarello, and R. Car, *Phys. Rev. Lett.* **89**, 245504 (2002).
- [27] M. Murakami *et al.*, *Phys. Rev. B* **99**, 045153 (2019).
- [28] S. K. Lee, *Proc. Natl. Acad. Sci. USA* **108**, 6847 (2011).
- [29] R. E. Cohen, in *High-Pressure Research: Application to Earth and Planetary Sciences*, edited by Y. Syono, and M. H. Manghnani (Terra Scientific Publishing Company (TERRAPUB), Tokyo, 1992), pp. 425.

- [30] B. B. Karki, L. Stixrude, and J. Crain, *Geophys. Res. Lett.* **24**, 3269 (1997).
- [31] M. Murakami, K. Hirose, S. Ono, and Y. Ohishi, *Geophys. Res. Lett.* **30**, 1207 (2003).
- [32] T. Tsuchiya, R. Caracas, and J. Tsuchiya, *Geophys. Res. Lett.* **31**, L11610 (2004).
- [33] S. Petitgirard *et al.*, *Phys. Rev. Lett.* **119**, 215701 (2017).
- [34] S. K. Lee and E. J. Kim, *J. Phys. Chem. C* **119**, 748 (2015).
- [35] S.-Y. Xie *et al.*, *J. Phys. Chem. Lett.* **9**, 2388 (2018).
- [36] S. K. Lee and S. Ryu, *J. Phys. Chem. Lett.* **9**, 150 (2018).
- [37] T. Sato and N. Funamori, *Phys. Rev. Lett.* **101**, 255502 (2008).
- [38] M. O'Keefe and B. G. Hyde, *Nature* **309**, 411 (1984).
- [39] M. O'Keefe and B. G. Hyde, in *Structure and Bonding in Crystals*, edited by M. O'Keefe, and A. Navrotsky (Academic Press, 1981), pp. 227.
- [40] M. O'Keefe and B. G. Hyde, *J. Solid State Chem.* **44**, 24 (1982).
- [41] A. I. Chumakov *et al.*, *Phys. Rev. Lett.* **112**, 025502 (2014).
- [42] E. Ohtani, *Chem. Geol.* **418**, 6 (2015).
- [43] Y. F. Duan, N. Y. Sun, S. H. Wang, X. Y. Li, X. Guo, H. W. Ni, V. B. Prakapenka, and Z. Mao, *Earth Planet. Sci. Lett.* **494**, 92 (2018).
- [44] J. Liu *et al.*, *Nature* **551**, 494 (2017).
- [45] D. B. Ghosh, B. B. Karki, and L. Stixrude, *Am. Mineral.* **99**, 1304 (2014).
- [46] L. Stixrude and B. Karki, *Science* **310**, 297 (2005).
- [47] I. Ohira, M. Murakami, S. Kohara, K. Ohara, and E. Ohtani, *Prog. Earth Planet. Sci.* **3**, 18 (2016).
- [48] See Supplemental Material, which includes Refs. [49-76]
- [49] J. R. Allwardt, J. F. Stebbins, B. C. Schmidt, D. J. Frost, A. C. Withers, and M. M. Hirschmann, *Am. Mineral.* **90**, 1218 (2005).
- [50] S. K. Lee, *Solid State Nucl. Magn. Reson.* **38**, 45 (2010).
- [51] S. K. Lee, G. D. Cody, Y. W. Fei, and B. O. Mysen, *Geochim. Cosmochim. Acta* **68**, 4189 (2004).
- [52] S. K. Lee, Y. S. Yi, G. D. Cody, K. Mibe, Y. W. Fei, and B. O. Mysen, *J. Phys. Chem. C* **116**, 2183 (2012).
- [53] X. Xue, J. F. Stebbins, and M. Kanzaki, *Am. Mineral.* **79**, 31 (1994).
- [54] J. L. Yarger, K. H. Smith, R. A. Nieman, J. Diefenbacher, G. H. Wolf, B. T. Poe, and P. F. McMillan, *Science* **270**, 1964 (1995).
- [55] G. H. Wolf and P. F. McMillan, in *Structure, Dynamics, and Properties of Silicate Melts*, edited by J. F. Stebbins, P. F. McMillan, and D. B. Dingwell (Mineralogical Society of America, Washington, D.C., 1995), pp. 505.
- [56] J.-L. Barrat, J. Badro, and P. Gillet, *Mol. Simul.* **20**, 17 (1997).
- [57] J. S. Tse, D. D. Klug, and Y. Le Page, *Phys. Rev. B* **46**, 5933 (1992).
- [58] A. Zeidler *et al.*, *Phys. Rev. B* **90**, 024206 (2014).
- [59] S. K. Lee, *J. Phys. Chem. B* **108**, 5889 (2004).
- [60] J. F. Stebbins, *Am. Mineral.* **101**, 753 (2016).
- [61] J. F. Stebbins and X. Y. Xue, in *Spectroscopic Methods in Mineralogy and Materials Sciences*, edited by G. S. Henderson, D. R. Neuville, and R. T. Downs (Mineralogical Society of America, Washington, D.C., 2014), pp. 605.
- [62] S. K. Lee, K. Mibe, Y. W. Fei, G. D. Cody, and B. O. Mysen, *Phys. Rev. Lett.* **94**, 165507 (2005).
- [63] W. L. Mao *et al.*, *Science* **302**, 425 (2003).
- [64] Y. Meng *et al.*, *Proc. Natl. Acad. Sci. USA* **105**, 11640 (2008).

- [65] B. J. A. Moulton, G. S. Henderson, H. Fukui, N. Hiraoka, D. de Ligny, C. Sonnevile, and M. Kanzaki, *Geochim. Cosmochim. Acta* **178**, 41 (2016).
- [66] W. Schulke, in *Electron Dynamics by Inelastic X-ray Scattering* (Oxford University Press 2007), p. 186.
- [67] Y. Lin, L. Zhang, H.-k. Mao, P. Chow, Y. Xiao, M. Baldini, J. Shu, and W. L. Mao, *Phys. Rev. Lett.* **107**, 175504 (2011).
- [68] H. Fukui, M. Kanzaki, N. Hiraoka, and Y. Q. Cai, *Phys. Chem. Miner.* **36**, 171 (2009).
- [69] S. K. Lee, P. J. Eng, H. K. Mao, Y. Meng, and J. Shu, *Phys. Rev. Lett.* **98**, 105502, 105502 (2007).
- [70] S. K. Lee, P. J. Eng, H. K. Mao, and J. F. Shu, *Phys. Rev. B* **78**, 214203 (2008).
- [71] S. K. Lee, S. Y. Park, H. I. Kim, O. Tschauner, P. Asimow, L. Bai, Y. Xiao, and P. Chow, *Geophys. Res. Lett.* **39**, L05306 (2012).
- [72] P. Blaha, Schwarz, K., Madsen, G., Kvasnicka, D and Luitz, J, WIEN2k, Techn. Univ. Wien, Austria, 2001.
- [73] J. P. Perdew, A. Ruzsinszky, G. I. Csonka, O. A. Vydrov, G. E. Scuseria, L. A. Constantin, X. Zhou, and K. Burke, *Phys. Rev. Lett.* **100**, 136406 (2008).
- [74] G. Will, M. Bellotto, W. Parrish, and M. Hart, *J. Appl. Crystallogr.* **21**, 182 (1988).
- [75] T. Yamanaka, T. Fukuda, and J. Mimaki, *Phys. Chem. Miner.* **29**, 633 (2002).
- [76] D. M. Teter, R. J. Hemley, G. Kresse, and J. Hafner, *Phys. Rev. Lett.* **80**, 2145 (1998).

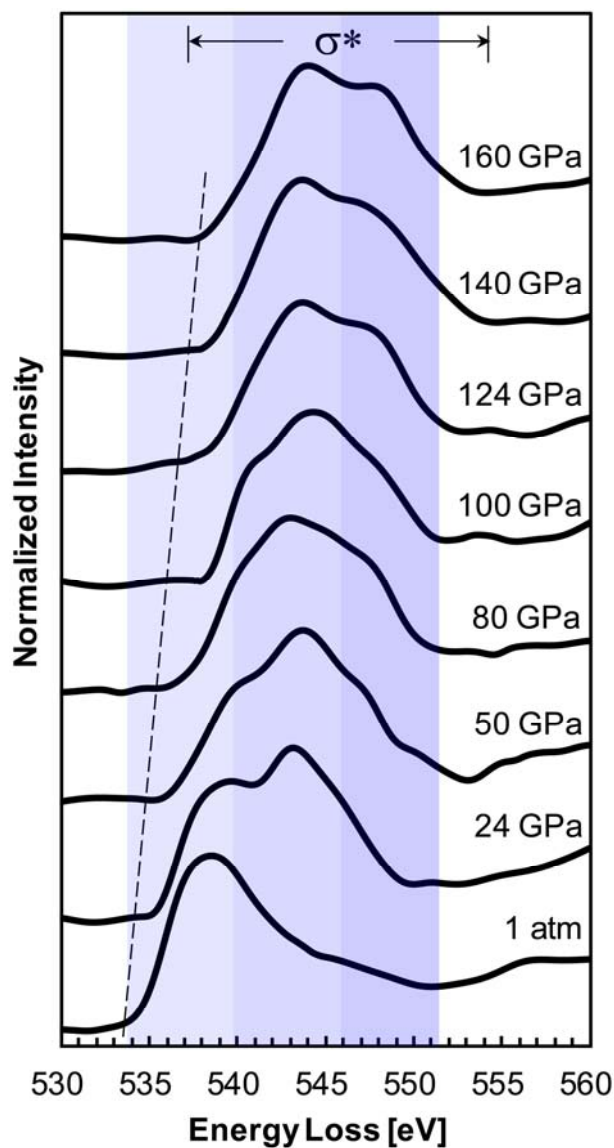


Figure 1 | Oxygen K-edge XRS spectra of SiO₂ glass at pressures up to ~160 GPa plotted as the normalized scattered photon intensity *vs.* the energy loss (incident energy - elastic energy). See Figure S2 for the XRS spectra without smoothing in accordance with the spectral uncertainty.

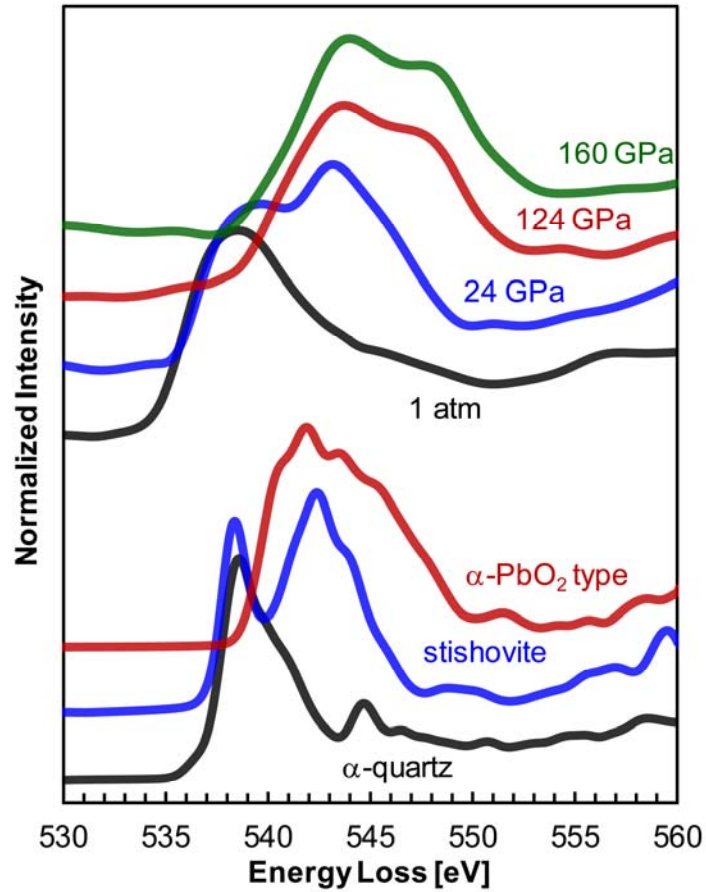


Figure 2 | Calculated oxygen *K*-edge XRS spectra for α -quartz (1 atm), stishovite (~ 29.1 GPa), and α -PbO₂-type SiO₂ (~ 120 GPa) with the Gaussian broadening factor of 1 eV (S6 for the calculation methods). The *K*-edge XRS spectra of a-SiO₂ under similar pressure conditions and that at 160 GPa are shown for comparison.

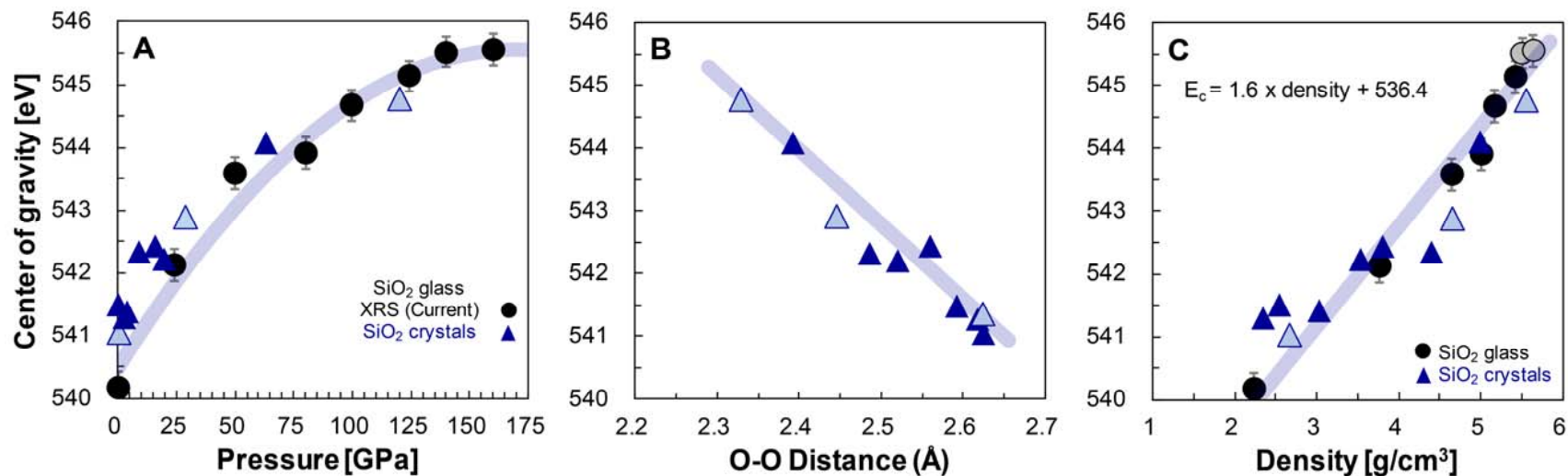


Figure 3 | a. Variation of the edge energy at the center of gravity (E_c) in the oxygen K -edge XRS spectrum for a- SiO_2 (black circles) with varying pressure. The E_c values for crystalline silica polymorphs are also shown (blue triangles). The pale blue symbols are based on the three polymorphs shown in Figure 2 (S6). b. E_c values of crystalline SiO_2 phases with varying O-O distances. c. Relationship between E_c and density for crystalline and amorphous SiO_2 . The densities of the a- SiO_2 glasses were from a recent experiment[33].

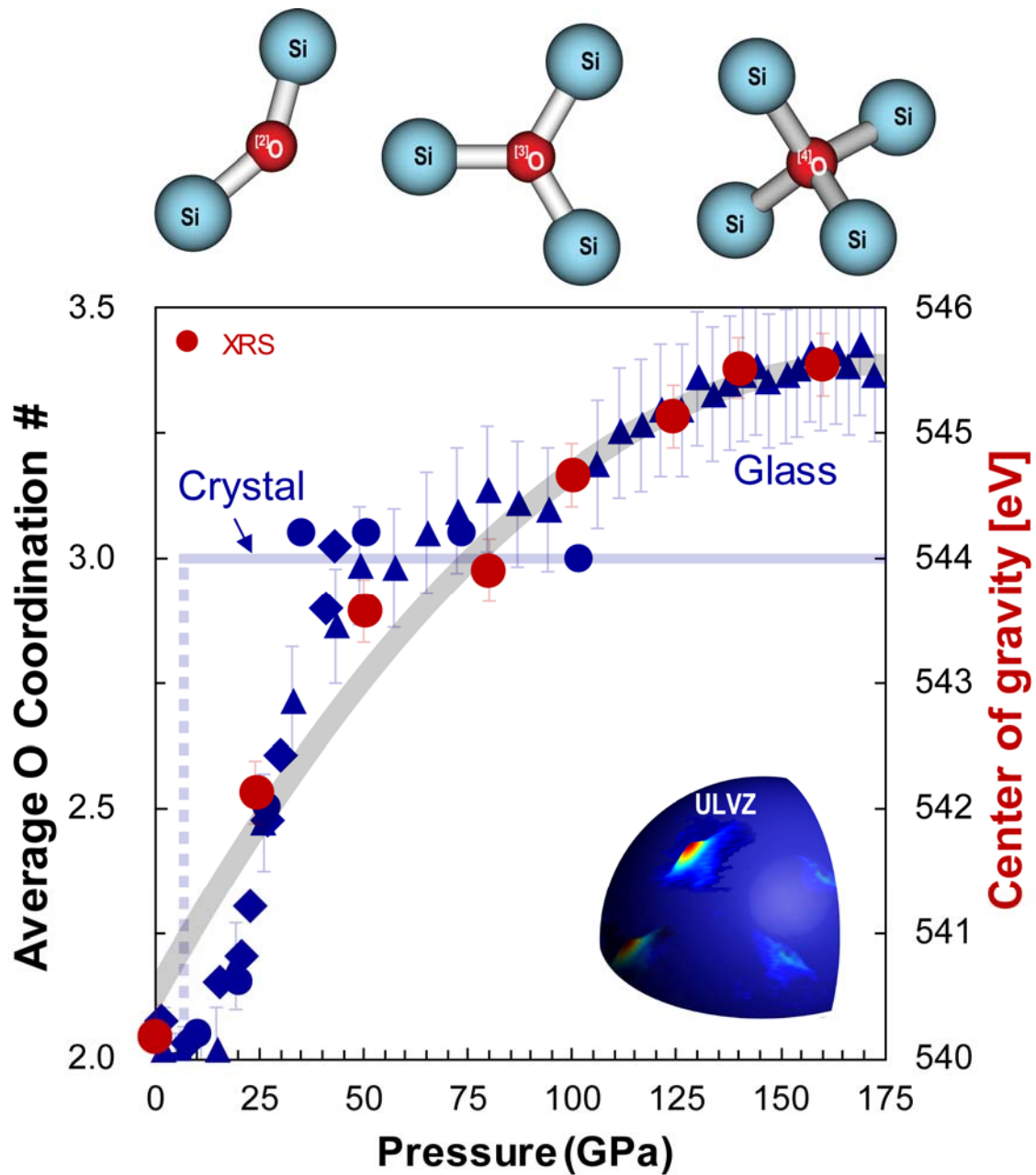


Figure 4 | Changes in the *average* oxygen coordination number (C_O) and E_c of SiO_2 glass up to 160 GPa. The C_O values are calculated from the average silicon coordination numbers (C_{Si}) from previous studies [blue circle[13]; blue diamond[11]; blue triangle[12]; red circle (current study) based on E_c in figure 3, S2]. Schematics of the oxygen configurations with varying coordination numbers (top) and ultra-low velocity zone (ULVZ) at the lower mantle are shown.